

# Microstructure Sensitive Fatigue Crack Nucleation in Titanium Alloys Using Accelerated Crystal Plasticity FE Simulations

Somnath Ghosh and Pritam Chakraborty

**Abstract** This chapter investigates microstructure and load sensitive fatigue behavior of Ti-6242 using cyclic crystal plasticity finite element (CPFE) simulations of statistically equivalent image-based microstructures. A wavelet transformation induced multi-time scaling (WATMUS) method (Joseph et al., *Comput Methods Appl Mech Eng* 199:2177–2194, 2010; Chakraborty et al., *Finite Elem Anal Des* 47:610–618, 2011; Chakraborty and Ghosh, *Int J Numer Methods Eng* 93:1425–1454, 2013; Ghosh and Chakraborty, *Int J Fatigue* 48:231–246, 2013) is used to perform accelerated cyclic CPFE simulations till crack nucleation, otherwise infeasible using conventional time integration schemes. A physically motivated crack nucleation model in terms of crystal plasticity variables (Anahid et al., *J Mech Phys Solids* 59(10):2157–2176, 2011) is extended in this work to predict nucleation. The dependence of yield strength on the underlying grain orientations and sizes is developed through the introduction of an effective microstructural parameter *Plastic Flow Index* or *PFI*. To determine the effects of the microstructure on crack nucleation, a local microstructural variable is defined in terms of the surface area fraction of soft grains surrounding each hard grain or *SAFSSG*. Simulations with different cyclic load patterns suggest that fatigue crack nucleation in Ti-6242 strongly depends on the dwell cycle hold time at maximum stress.

## 1 Introduction

The fatigue life and number of cycles to crack nucleation in commercially used titanium alloys, such as Ti-6242, exhibit considerable variation at room temperature due to the heterogeneity of the underlying microstructure [2, 16, 17]. Mechanistic

---

S. Ghosh (✉)

Department of Civil Engineering, Johns Hopkins University, 3400 N. Charles Street, Baltimore, MD 21218, USA

e-mail: [sghosh20@jhu.edu](mailto:sghosh20@jhu.edu)

P. Chakraborty

Idaho National Laboratory, Idaho Falls, ID, USA

e-mail: [pritam.chakraborty@inl.gov](mailto:pritam.chakraborty@inl.gov)

approaches, implementing crystal plasticity-based finite element (CPFEM) simulations of polycrystalline microstructures, have been pursued in the literature [3, 8, 13–16] to develop fatigue life models. At room temperature, inelastic deformation in Ti-6242 commences predominantly by slip on different slip systems in individual grains of the microstructure [2, 17]. The number of slip systems and their resistance to slip depends on the morphological and crystallographic characteristics. In the *hcp* phase of Ti-6242, the three basal and prismatic  $\langle a \rangle$  slip systems have much lower slip resistances in comparison with the 6  $\langle a \rangle$  pyramidal, 12  $\langle c + a \rangle$  first order pyramidal and 6  $\langle c + a \rangle$  second order pyramidal slip systems [6, 11]. Consequently, grains with orientations that induce higher resolved shear stresses on the basal or prismatic systems have more plastic deformation than those activating the pyramidal systems. This material anisotropy due to the large difference in critical resolved shear stress in different slip systems results in large heterogeneity in the plastic deformation in polycrystalline aggregates. It leads to significant load-shedding induced stress concentration at grain boundaries. This is perceived to be the primary driver of microstructure-dependent crack nucleation [2].

The present work uses a size and rate-dependent CPFEM model of Ti-6242 developed in [6, 11, 19] to capture this load-shedding induced stress rise in the microstructure leading to crack nucleation. Particularly vulnerable are boundaries between grains having large time-dependent plastic deformation (soft grain) and those with little or no plasticity (hard grain) owing to their orientation with respect to the loading direction. Morphological and crystallographic features of the polycrystalline alloy are statistically represented in the CPFEM models using methods developed in [9, 10]. The use of such a statistical description not only reduces the number of grains in the FE simulations but also captures the key features of the microstructure that affect its macroscopic and microscopic response. A non-local crack nucleation model has been developed in [1] to study early crack nucleation in polycrystalline Ti-alloys under dwell fatigue cyclic loading. The crack nucleation criterion is functionally dependent on stress concentration and dislocation pile-up at grain boundaries. These variables are obtained from CPFEM simulations. A combination of CPFEM simulations and ultrasonic testing of dwell fatigue Ti-6242 samples has been used in [1] for calibrating and validating the nucleation model. This model is adopted in the present work to study microstructure and load-dependent crack nucleation in Ti-6242.

Although CPFEM simulations accurately capture the deformation behavior of polycrystalline alloys, they require very small time steps when conventional time integration schemes are used to march forward in time. In cyclic loading and deformation, small time steps in every cycle of the loading process leads to prohibitively large computations, when analysis is performed for a large number of cycles to fatigue failure. The *wavelet transformation induced multi-time scaling* or WATMUS method, developed in [4, 5, 7, 12], has shown significant computational benefits in rapidly traversing a high number of cycles. This chapter discusses the effects of microstructure and cyclic loading conditions on grain-level crack nucleation.

The WATMUS method based cyclic CPFÉ simulations of polycrystalline Ti-6242 microstructures are used to accomplish this mechanistic approach. A detailed numerical study of the different factors affecting fatigue crack nucleation in Ti-6242 is executed in Sect. 5. In Sect. 5.1, relations between crystallographic features and cycles to crack nucleation are developed. The dependence on the number of cycles to crack nucleation on characteristics of the applied load is studied in Sect. 5.2.

## 2 Rate-Dependent Crystal Plasticity and Nonlocal Crack Evolution Models for Ti-6242

The rate and size-dependent crystal plasticity constitutive laws governing deformation in polycrystalline, bi-phasic Ti-6242 alloys have been detailed in [6, 11, 19]. A power law model is used to determine the slip-rate on different slip systems as:

$$\dot{\gamma}^\alpha = \dot{a} \left| \frac{\tau^\alpha - \chi^\alpha}{g^\alpha} \right|^{\frac{1}{m}} \text{sign}(\tau^\alpha - \chi^\alpha) \quad (1)$$

where  $\dot{a}$  is a reference slip rate,  $\tau^\alpha$  is the resolved shear stress on the slip system,  $\chi^\alpha$  is a back stress,  $g^\alpha$  is the slip system resistance, and  $m$  is the power law exponent. The resolved shear stress on a slip system is obtained from the relation

$$\tau^\alpha = \mathbf{F}^e \mathbf{T} \mathbf{F}^e \mathbf{T}^* : \mathbf{S}_0^\alpha \quad (2)$$

where  $\mathbf{T}^*$  is the second Piola–Kirchhoff (PK2) stress. The back stress evolution on a slip system follows the law:

$$\dot{\chi}^\alpha = c \dot{\gamma}^\alpha - d \chi^\alpha |\dot{\gamma}^\alpha| \quad (3)$$

where  $c$  and  $d$  are the direct hardening and dynamic recovery coefficients, respectively. The evolution of slip system deformation resistance is controlled by two types of dislocations, viz., statistically stored dislocations (SSDs) and geometrically necessary dislocations (GNDs) [1]. The corresponding deformation resistance rate is expressed as:

$$\dot{g}^\alpha = \sum_{\beta} h^{\alpha\beta} |\dot{\gamma}^\beta| + \frac{k_0 \hat{\alpha}^2 G^2 b}{2(g^\alpha - g_0^\alpha)} \sum_{\beta} \lambda^\beta |\dot{\gamma}^\beta| \quad (4)$$

The modulus  $h^{\alpha\beta} = q^{\alpha\beta} h^\beta$  (no sum on  $\beta$ ) is the strain hardening rate due to self and latent hardening on the  $\alpha$ -th slip system by slip on the  $\beta$ -th slip system, respectively. Here,  $h^\beta$  is the self hardening coefficient and  $q^{\alpha\beta}$  is a matrix describing latent hardening. Different self hardening relationships are used for modeling the  $\alpha$

and  $\beta$  phases [6]. The evolution of self hardening for the  $\alpha$  phase is modeled as:

$$h^\alpha = h_0^\alpha \left| 1 - \frac{g^\alpha}{g_s^\alpha} \right|^r \text{sign} \left( 1 - \frac{g^\alpha}{g_s^\alpha} \right), \quad g_s^\alpha = \tilde{g} \left| \frac{\dot{\gamma}^\alpha}{\dot{a}} \right|^c \quad (5)$$

where  $h_0^\alpha$  is a reference self hardening parameter and  $g_s^\alpha$  is the saturation value of slip system resistance. Self hardening rate of the  $\beta$  phase is given as:

$$h^\alpha = h_s^\alpha + \text{sech}^2 \left[ \frac{h_0^\alpha - h_s^\alpha}{\tau_s^\alpha - \tau_0^\beta} \gamma^{acc} \right] (h_0^\alpha - h_s^\alpha) \quad \text{where} \quad \gamma^{acc} = \int_0^t \sum_\alpha |\dot{\gamma}^\alpha| dt \quad (6)$$

$h_0^\alpha$  and  $h_s^\alpha$  are the initial and the asymptotic hardening rates,  $\tau_s^\alpha$  represents the saturation value of shear stress when  $h_s^\alpha = 0$ , and  $\gamma^{acc}$  is the accumulated plastic slip. The second term in Eq. (4) accounts for the effect of GNDs on work hardening. Here,  $k_0$  is a dimensionless material constant,  $G$  is the elastic shear modulus,  $b$  is the Burgers vector,  $g_0^\alpha$  is the initial deformation resistance, and  $\hat{a}$  is a non-dimensional constant.  $\hat{a}$  is taken to be  $\frac{1}{3}$  in [1].  $\lambda^\beta$  is a measure of slip plane lattice incompatibility, which can be expressed for each slip system as a function of slip plane normal  $\mathbf{n}^\beta$  and an incompatibility tensor  $\Lambda$  as:

$$\lambda^\beta = \Lambda \mathbf{n}^\beta : \Lambda \mathbf{n}^\beta)^{\frac{1}{2}} \quad (7)$$

The dislocation density tensor  $\Lambda$  can be expressed using the curl of plastic deformation gradient tensor  $\mathbf{F}^P$ .

The effect of grain size and lath thickness on the slip system resistance is also considered in the crystal plasticity model in [19]. A Hall Petch type relation is used to modify the initial slip system resistances  $g^\alpha(t = 0)$  to capture size effect according to the relation:

$$g^\alpha(t = 0) = g_0^\alpha + \frac{K^\alpha}{\sqrt{D^\alpha}} \quad (8)$$

where  $g_0^\alpha$  is the homogeneous slip system resistance,  $D^\alpha$  is a characteristic length parameter that corresponds to the mean-free path of the dislocations in a grain. For globular  $\alpha$  grains, the transmission of dislocations to adjacent grains is resisted by grain boundaries and hence grain diameter is considered as characteristic length in Eq. (8). For transformed  $\beta$  colonies, dislocation motions can be impeded either by the colony boundary or lath boundary depending on the Burger's orientation relation between  $\alpha$  and  $\beta$  laths [6, 11]. Hence either colony size or lath thickness is used for  $D^\alpha$  in Eq. (8) for slip system resistances of the transformed  $\beta$  colonies.  $K^\alpha$  is a constant that depends on the Poisson's ratio, shear modulus, Burgers vector, and barrier strength.

A crack nucleation model, developed in [1], is used in this work to model grain-level nucleation in a polycrystalline ensemble. Experimentally extracted crystallographic features of grains at failure sites suggest that regions of hard grains surrounded by soft grains are susceptible to initiate a crack. Contiguous hard grains with less-favorably oriented for  $\langle a \rangle$ -type slip ( $\langle c \rangle$ -axis parallel to the deformation direction), experience large local stress concentrations, especially near the shared grain boundary. This is a consequence of compatible, large elastic strains in the hard grains near the shared boundary. The phenomenon of rising stress-concentration with evolving creep strains in dwell cycles has been called load shedding [1, 11]. The hard grain crack nucleation criterion, ahead of dislocation pile-ups in adjacent soft grain has been derived to be [1]:

$$T_{eff} = \sqrt{\langle T_n \rangle^2 + \beta T_t^2} \geq \frac{K_c}{\sqrt{\pi c}} \quad (9)$$

or equivalently

$$R = T_{eff} \cdot \sqrt{c} \geq R_c, \quad \text{where } R_c = \frac{K_c}{\sqrt{\pi}} \quad (10)$$

In Eqs. (9) and (10),  $T_{eff}$  is an effective traction on the hard grain basal plane for mixed mode crack nucleation. It is expressed in terms of the stress component normal to the crack surface  $T_n = \sigma_{ij} n_i^b n_j^b$  and the tangential stress component  $T_t = \|\mathbf{T} - T_n \mathbf{n}^b\|$ . Here  $\mathbf{T}$  is the stress vector on the crack surface,  $\sigma_{ij}$  is the Cauchy stress tensor, and  $n_i^b$  are the components of unit outward normal to the crack surface. Only the tensile normal stress  $\langle T_n \rangle$ , represented by the McCauley bracket  $\langle \rangle$ , contributes to the effective stress responsible for crack opening.  $K_c$  is the critical mixed-mode stress intensity factor and  $\beta \approx K_{nc}/K_{tc}$  is a shear stress factor used to assign different weights to the normal and shear traction components for mixed-mode. A value of  $\beta = 0.7071$  is used for Ti-64 alloys in this study.  $c$  is the length of a wedge micro-defect or crack on the basal plane of the hard grain caused by dislocation pile-up in the adjacent soft grain. The micro-crack length  $c$  in Eq. (10) is obtained from the relation proposed in [18] as:

$$c = \frac{G}{8\pi(1-\nu)\gamma_s} B^2 \quad (11)$$

where  $B$  is the crack opening displacement,  $G$  is the shear modulus,  $\nu$  is the Poisson's ratio, and  $\gamma_s$  is the surface energy. The crack opening displacement  $B = \|\mathbf{B}\|$  is a non-local variable. The critical crack nucleation parameter  $R_c$  in Eq. (10) is a material property, which is calibrated from experiments.

### 3 Wavelet Transformation Based Multi-time Scale Method for Accelerated Cyclic CPFEM Simulations

Fatigue life predictions in polycrystalline metallic microstructures involve cyclic crystal plasticity FEM simulations till crack nucleation. Depending on the microstructure and load profile, this may involve simulations for large number of cycles. Such simulations may become computationally prohibitive using conventional time integration schemes in FEM codes. In [4, 5, 7, 12], a wavelet transformation based multi-time scale or WATMUS method has been developed to reduce the problem to a set of low frequency, coarse time-scale governing equations. In the WATMUS scheme, any time-dependent variable  $v^\zeta(t)$  is expressed as:

$$v^\zeta(t) = v(N, \tau) = \sum_{k=1}^n v_k(N) \psi_k(\tau) \quad \forall \quad \tau \in [0, T] \quad (12)$$

The superscript  $\zeta$  corresponds to the dependence of the variable on the two time-scales, which for this problem correspond to a cycle scale  $N$  and an intra-cycle fine time-scale  $\tau$ .  $\psi_k(\tau)$  are wavelet basis functions that capture the high frequency response within each cycle,  $n$  is the number of basis functions required for accurate representation of the waveform. The finite support of the wavelet basis functions eliminates spurious oscillations that may arise with truncation of terms in infinitely supported basis functions such as the spectral basis functions.  $v_k(N)$  are the associated coefficients that evolve monotonically in the cycle ( $N$ )-scale. Using orthogonality property, they may be expressed as:

$$v_k(N) = \frac{1}{T} \int_0^T v(N, \tau) \psi_k(\tau) d\tau \quad (13)$$

where  $T$  is the time period of the applied load. Wavelet transformation facilitates numerical integration of the CPFEM equations in the cycle-scale traversing several cycles in each step. This leads to significant efficiency gain.

The oscillatory stress response  $\sigma_{ji}(N, \tau)$  depends on the oscillatory deformation gradient  $F_{ij}(N, \tau)$  and internal variables  $y_m(N, \tau)$ .  $F_{ij}(N, \tau)$  at each integration point in any cycle is obtained from the coefficients of nodal displacements  $C_{i,k}^\alpha(N)$  using the relation:

$$F_{ij}(N, \tau) = \delta_{ij} + \frac{\partial P^\alpha}{\partial X_j} \sum_{k=1}^n C_{i,k}^\alpha(N) \psi_k(\tau) \quad (14)$$

In crystal plasticity, the evolution of internal variables is governed by first order rate equations of the type

$$\dot{y}_m^\zeta(t) = f_m(y_m^\zeta, F_{ij}^\zeta, t) \quad (15)$$

Here  $y_m^\xi$  are internal variables represented in a single time-scale,  $t$  and  $f_m$  are non-linear functions. The oscillatory evolution of the dual-scale variable  $y_m(N, \tau)$  in any cycle may be obtained from the fine-scale time integration as:

$$y_m(N, \tau) = y_{m0}(N) + \int_0^\tau f_m(y_m, F_{ij}, N, \tau) d\tau \quad (16)$$

where  $y_{m0}(N) = y_m(N, \tau = 0)$  are values of internal variables at the beginning of a cycle. This forms a new cycle-scale variable, corresponding to the initial values of internal variables  $y_{m0}$ , which have a monotonic evolution in the cycle-scale. Cycle-scale rate equations are numerically defined for  $y_{m0}$  as [12]:

$$\frac{\partial y_{m0}}{\partial N} = y_{m0}(N + 1) - y_{m0}(N) = y_m(N, T) - y_{m0}(N) \quad (17)$$

where

$$y_m(N, T) = y_{m0}(N) + \int_0^T f_m(y_m, F_{ij}, N, \tau) d\tau \quad (18)$$

Since  $f_m$  are non-linear functions, numerical time-integration using the backward Euler scheme is performed on Eq. (18). The cycle-scale internal variables are integrated using a second order backward difference formula, expressed as:

$$y_{m0}(N) = \beta_1 y_{m0}(N - \Delta N) - \beta_2 y_{m0}(N - \Delta N - \Delta N_p) + \beta_3 \left. \frac{\partial y_{m0}}{\partial N} \right|_N \Delta N$$

$$\text{where } \beta_1 = \frac{(r+1)^2}{(r+1)^2 - 1} \quad \beta_2 = \frac{1}{(r+1)^2 - 1} \quad \beta_3 = \frac{(r+1)^2 - (r+1)}{(r+1)^2 - 1}$$

$$\text{and } r = \frac{\Delta N_p}{\Delta N} \quad (19)$$

The Newton–Raphson iterative scheme is used to solve Eq. (19).

The accuracy of the WATMUS method is demonstrated by comparing the evolution of crystal plasticity variables obtained from (1) single time-scale, and (2) WATMUS method-enhanced dual time-scale simulations of a statistically equivalent virtual polycrystalline Ti-6242 microstructure [9, 10]. In Fig. 1, the microstructure is subjected to a triangular cyclic load on the y-face with a maximum and minimum normal traction of 869 MPa and 0 MPa respectively, and a time period of 2 s. The WATMUS method-enhanced CPFEM simulation is performed for 300,000 cycles and the evolutionary variables, e.g. set of wavelet coefficients of nodal displacements  $C_{i,k}^\alpha$  and the history of coarse scale internal variables  $\mathbf{y}_0^{\alpha/\beta} = \{F_{ij,0}^\beta, g_0^\alpha, \chi_0^\alpha\}$  are compared with a single time-scale simulation. The single time-scale simulation

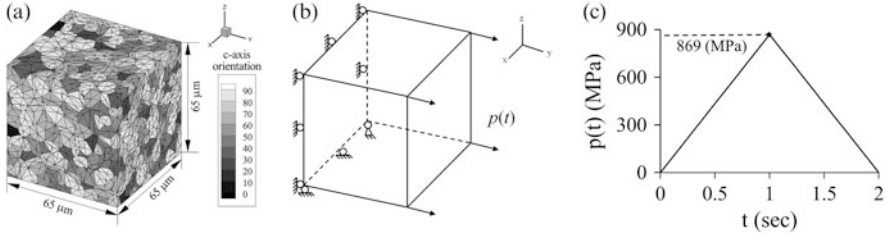


**Fig. 1** FE model of a polycrystalline microstructure and loading conditions to demonstrate the accuracy and efficiency of the WATMUS method: (a) microstructure with  $\langle c \rangle$ -axis orientation and mesh, (b) boundary conditions, and (c) cyclic loading profile

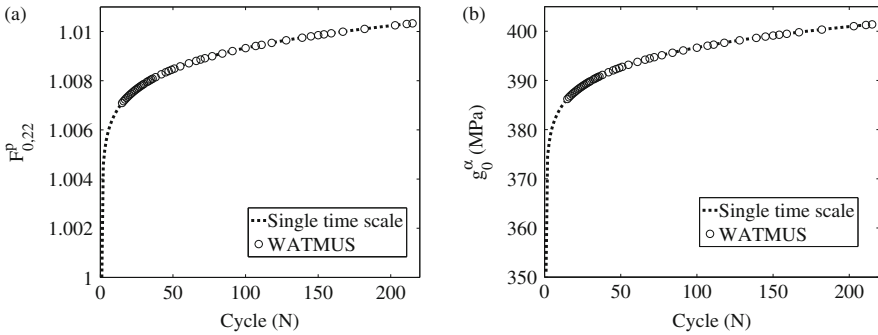


**Fig. 2** Comparison of the evolution of the cycle-scale with averaged single time-scale internal variables at an integration point in the FE model of the polycrystalline microstructure for: (a)  $F_{0,22}^p$ , (b)  $g_0^\alpha$

suffers from a large computational overhead, and the simulation is performed for 215 cycles only. A comparison of the evolution of coarse internal variables at an integration point in the microstructure is shown in Fig. 2.

The distribution of the loading direction stress  $\sigma_{22}$  along a specified material line in the microstructure, as obtained by the WATMUS and single time-scale simulations is compared in the Fig. 3. These comparisons conclusively show that the WATMUS method is able to capture the evolution of the local microstructural variables very accurately. Finally to demonstrate the power of the WATMUS method in traversing a large number of cycles, the evolution of plastic deformation gradient  $F_{0,22}^p$  with advancing cycles are shown in Fig. 4 for up to 300,000 cycles. To evaluate the computational efficiency, the CPU time to perform 215 cycles for the single time-scale CPFEM simulation is extrapolated to 300,000 cycles and compared with the CPU time taken to perform 300,000 cycles of WATMUS simulation. A computational speedup of  $\sim 100$  times is obtained for this problem.



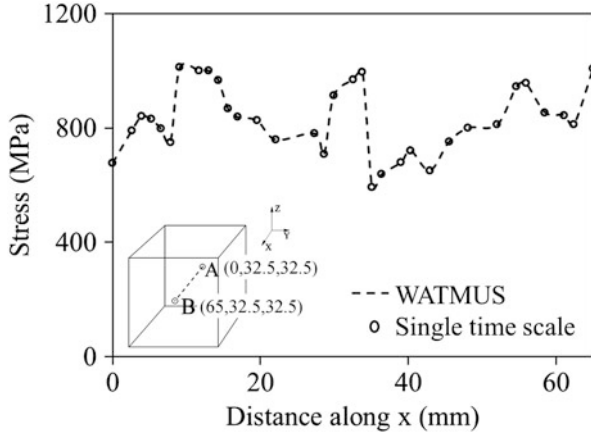


**Fig. 3** Comparison of distribution of stress  $\sigma_{22}$  along a material line in the microstructure at  $N = 211$  and  $\tau = 1$  s, by the WATMUS and single time-scale CPFEM simulations for  $\sigma_{22}$

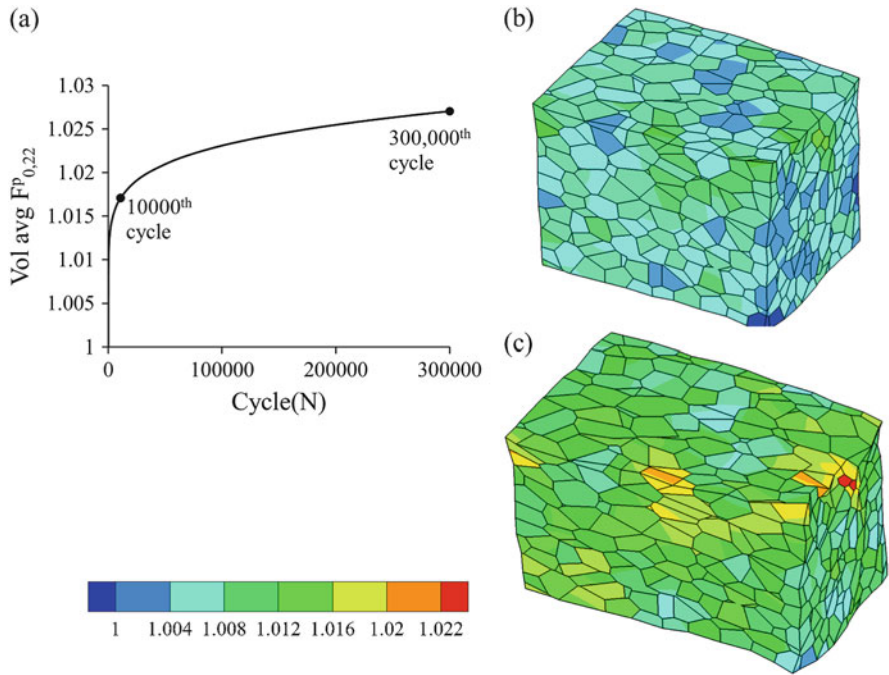


**Fig. 4** Evolution of  $F_{0,22}^p$  with cycles by WATMUS-based CPFEM simulation: (a) volume averaged  $F_{0,22}^p$ , (b) distribution of  $F_{0,22}^p$  at the 10,000th cycle, and (c) distribution of  $F_{0,22}^p$  at the 300,000th cycle

### 3.1 WATMUS Method Based Dwell Fatigue Simulation of Ti-6242 Microstructure

The ability of the WATMUS method in handling large time periods is demonstrated through a dwell fatigue simulation for the polycrystalline microstructure shown in Fig. 1. A schematic of the dwell load with 2 min hold and the corresponding segments are shown in Fig. 5a, b, respectively.

The cycle-scale evolution of  $F_{0,22}^p$  and  $g_0^\alpha$  for a slip system at an integration point in the microstructure by the WATMUS method-enhanced CPFEM simulation is shown in Fig. 6. The evolution of  $\sigma_{22}$  along a material line in the microstructure is evaluated for the cycles 21 and 500, at  $\tau = 121$  s, and is depicted in Fig. 7. Large stresses develop in the hard grains adjacent to soft grains due to anisotropy, leading to orientation dependent rate of plastic deformation and load-shedding. The stress peak rises with advancing cycles of the load, thus enhancing the probability

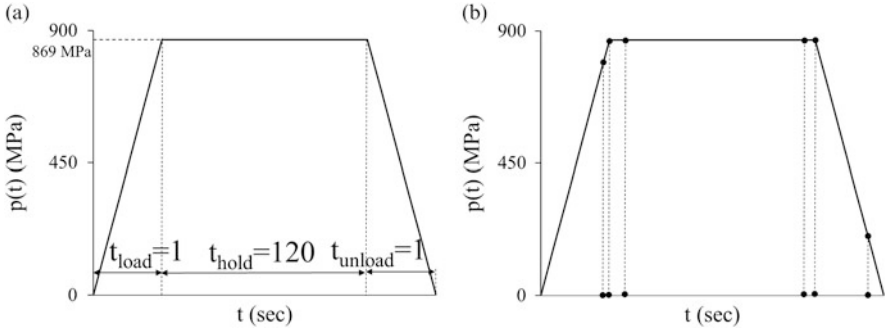


**Fig. 5** Schematic of cyclic dwell loading: (a) dwell load profile applied on  $y$ -face of the polycrystalline microstructure (b) segments with different maximum resolution

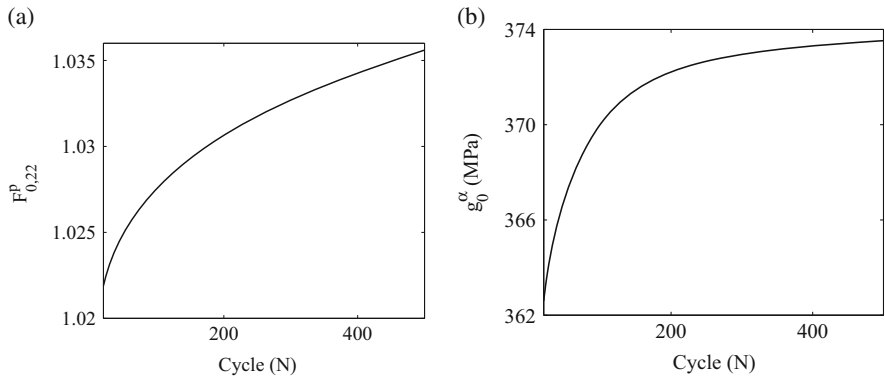


**Fig. 6** Evolution of cycle-scale internal variables at an integration point in the microstructure: (a)  $F_{0,22}^p$  (b) one of the slip system resistances  $g_0^\alpha$

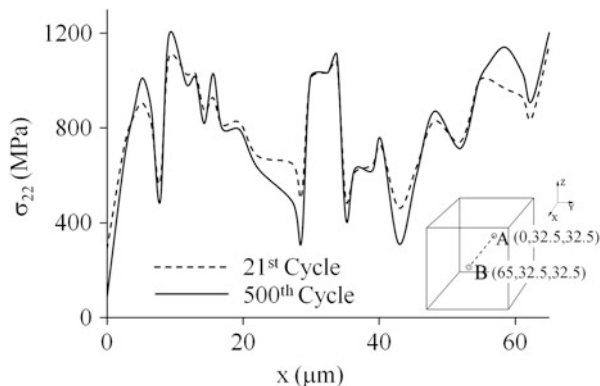


**Fig. 7** Evolution of loading direction stress component  $\sigma_{22}$  along a material line in the microstructure evaluated at cycles  $N = 21$  and  $N = 500$  and  $\tau = 121$  s

of crack nucleation in these hard grains. The WATMUS method-enhanced CPFE simulations are used in conjunction with the crack nucleation model to study the fatigue nucleation behavior of Ti-alloys.

#### 4 Calibration and Validation of Critical Crack Nucleation Parameter $R_c$

The critical crack nucleation parameter  $R_c$  should be calibrated prior to conducting crack nucleation sensitivity analyses using CPFE simulations. Validation studies are performed using two different specimens of the Ti-6242 alloy, subject to dwell fatigue load with a hold time of 2 min, and loading and unloading time of 1 s each. The maximum stress in a loading cycle is 869 MPa, which is 95 % of the yield strength, while the minimum stress is 0 MPa. Subsurface crack propagation has been monitored by using micro-radiographic images from interrupted experiments in [20]. From dwell fatigue experiments, it has been observed that crack nucleation occurs at 80–85 % of the total number of cycles to failure  $N_f$ . The overall yield strengths of the specimens 1 and 2 in the loading direction are evaluated from constant strain rate simulations prior to dwell fatigue simulations. Corresponding to 0.2 % elastic strain, an yield strength value of  $\sim 915$  MPa is assessed for these specimens.

The WATMUS method-enhanced CPFEM simulations are performed under dwell loading for validating the crack nucleation model. Consistent with experimental procedures, a maximum applied stress of 869 MPa, which corresponds to 95 % of the yield stress, and a stress ratio  $\sigma_R = \sigma_{min}/\sigma_{max} = 0$  is applied. Following the procedure described in [1], the crack nucleation parameter  $R_\alpha$  at every node on grain interfaces is evaluated at  $\tau = 121$  s in each cycle for the 2-min dwell. Experimental

results of specimen 1, which fails after 352 cycles, are used to calibrate  $R_c$ . From the conclusions of experimental studies in [20], the minimum and maximum number of cycles to crack nucleation for the specimen 1 is estimated as  $N_{c(80\%)} = 282$  (80 % of  $N_f$ ) and  $N_{c(85\%)} = 300$  (85 % of  $N_f$ ). The evolution of the nodal  $R_\alpha$  at the grain boundaries is obtained from CPFЕ simulations of specimen 1. The maximum  $R_\alpha$  values at  $N_{c(80\%)} = 282$  and  $N_{c(80\%)} = 300$  are considered as the lower and upper limits of  $R_c$ , respectively.

$$\begin{aligned} R_{c(80\%)} &= \max_{\alpha} R_{\alpha}(N = 282, \tau = 121 \text{ s}) = 6.54 \text{ MPa} \sqrt{\mu\text{m}} \\ R_{c(85\%)} &= \max_{\alpha} R_{\alpha}(N = 300, \tau = 121 \text{ s}) = 6.80 \text{ MPa} \sqrt{\mu\text{m}} \end{aligned} \quad (20)$$

Experimental results of specimen 2 are used to validate the crack nucleation model for the calibrated  $R_c$  value. The number of cycles to crack nucleation from interrupted dwell fatigue experiments is 550 cycles. From the CPFЕ simulations, the number of cycles to crack nucleation is predicted for 80 % and 85 %, respectively of the total life as:

$$\begin{aligned} N_{c(80\%)} : \max_{\alpha} R_{\alpha}(N, \tau = 121 \text{ s}) = R_{c(80\%)} &\Rightarrow N_{c(80\%)} = 620 \\ N_{c(85\%)} : \max_{\alpha} R_{\alpha}(N, \tau = 121 \text{ s}) = R_{c(85\%)} &\Rightarrow N_{c(85\%)} = 694 \end{aligned} \quad (21)$$

The evolution of maximum  $R_\alpha$  at a grain boundary node with crack nucleation is shown in Fig. 8.

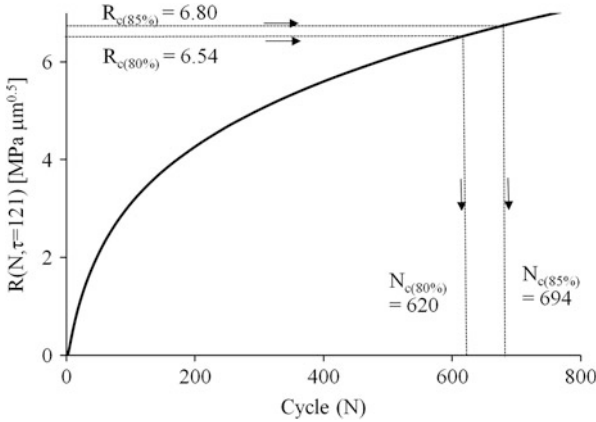


**Fig. 8** Evolution of maximum  $R_\alpha$  with  $N$  in specimen 2 at a crack nucleation site under dwell cyclic loading, evaluated at  $\tau = 121$  s

**Table 1** Comparison of the number of cycles to crack nucleation predicted by the model with experimental results for specimen 2

Cycles to crack nucleation (Experiment)	Cycles to crack nucleation (Predicted)		% Relative error	
	80 % of life	85 % of life	80 % of life	85 % of life
550	620	694	12.7	25.4

**Table 2** Crystallographic features of the crack nucleation site predicted by the model and experiments for specimens 1 and 2

Microstructural parameters	Experiments	Specimen 1	Specimen 2
$\theta_c$	0–30°	38.5°	25.2°
Prismatic Schmid factor	0.0–0.1	0.17	0.09
Basal Schmid factor	0.3–0.45	0.48	0.38

The predicted number of cycles to crack nucleation for specimen 2 along with the associated error are summarized in Table 1. The crystallographic features of the predicted crack nucleation site for both the specimens are compared with experimentally observed characteristics in Table 2.

## 5 Influence of Microstructural and Loading Characteristics on Crack Nucleation in Ti-6242

In this section, room temperature crack nucleation in Ti-6242 is related to microstructural features and loading profile under cyclic loading using the WATMUS method-enhanced CPFPE simulations. The yield strength of a polycrystalline alloy depends on the plastic flow behavior of the individual grains. Room temperature plastic deformation in Ti-6242 is primarily due to slip in individual grains. Consequently, factors affecting initiation of slip are used to study the sensitivity of yield strength to the underlying microstructure. Plastic deformation in a grain of a given size and orientation with the loading direction, is represented by a parameter termed as the *Plastic Flow Index* or *PFI*, defined as:

$$PFI = \max_{\alpha} \left( \frac{|\cos \theta_n^{\alpha} \cos \theta_m^{\alpha}|}{0.5} \right) \left( \frac{g_0^{prismatic}}{g^{\alpha}} \right) \quad (22)$$

where  $\theta_n^{\alpha}$  and  $\theta_m^{\alpha}$  are the angles made by the slip plane normals and the corresponding slip directions with the loading direction.  $g_0^{prismatic}$  is the slip system resistance of the prismatic  $\langle a \rangle$  slip system in Eq. (8). The calibrated value of  $g_0$  in [19] is the smallest for the prismatic  $\langle a \rangle$  slip system. Hence, it is considered as a reference in Eq. (22) since it implies least resistance to slip. A crystal oriented with the maximum Schmid factor 0.5 along the prismatic  $\langle a \rangle$  slip system has the minimum

yield strength and maximum plastic flow, compared to any other grain orientation. Thus the *PFI* is considered to provide an effective measure of plastic flow in the grain. It also depends on the loading direction or Schmid factor of individual slip systems in the grain. The *PFI* has characteristics similar to the Taylor factor in [17] in that it uses a measure of the slip rate to determine the degree of plasticity in each grain of the polycrystalline microstructure. However there are also some distinct differences, viz.

- The maximum ratio from all the slip systems in a grain is considered in *PFI*.
- The microstructure with maximum slip activity (single crystal with  $SF = 0.5$  on prismatic slip system) is considered to obtain the relative measure *PFI*.
- The distribution of *PFI* instead of a volume average is used to obtain a relative measure of yield strength for polycrystalline alloys.

For a grain, the value of *PFI* can vary between 0 and 1, i.e.,  $0 \leq PFI < 1$ . A higher value of *PFI*, i.e.,  $PFI \rightarrow 1$  indicates higher plastic flow and lower strength for the grain. The yield strengths of specimens 1 and 2 in the *y*-direction are related to the underlying grain sizes and orientations by considering the *PFI* distribution of individual grains in the microstructure. The distributions are compared in Fig. 9. The distributions show that both specimens 1 and 2 have similar high volume fractions ( $VF \approx 0.2$ ) in the range  $0.7 \leq PFI < 0.8$ . The *PFI* distribution provides an effective metric in relating the yield strength to the underlying grain sizes and orientations. To validate this postulate, a third virtual microstructure (specimen 3) is constructed by randomly assigning orientations to grains in the FE model of Fig. 1a. The orientations are chosen from the set of orientations in specimen 1. The grain sizes of specimen 3 are the same as for specimen 1. The *PFI* distribution for specimen 3 is compared with those for specimens 1 and 2 in Fig. 9. This has a lower volume fraction in the range  $0.7 \leq PFI < 0.8$ . Correspondingly, specimen 3 is

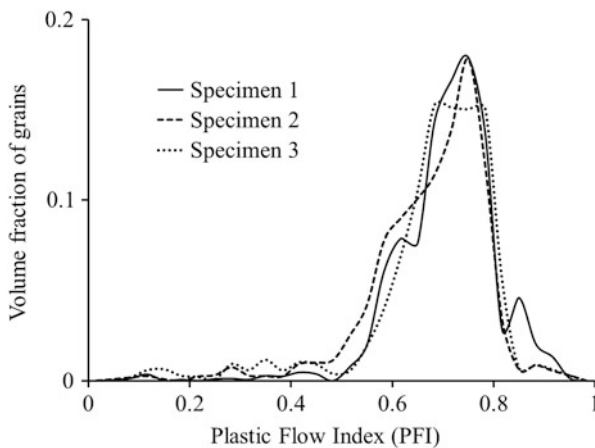


**Fig. 9** Plastic flow index (*PFI*) distribution for specimens 1–3

expected to have a higher yield strength. This is corroborated by constant strain-rate CPFЕ simulation results, for which the yield strength is 940 MPa.

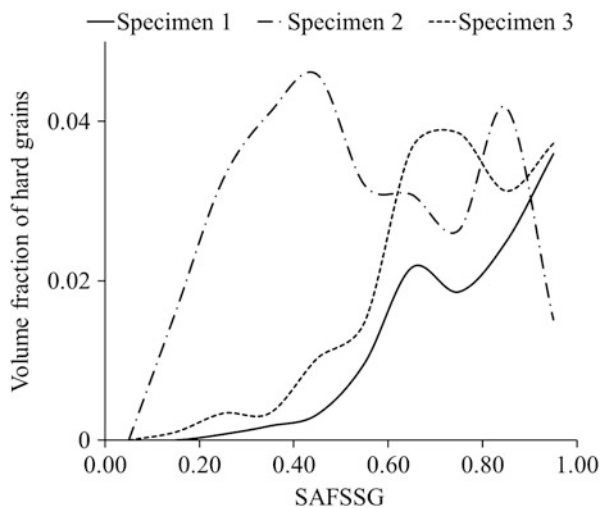
### 5.1 Sensitivity of Crack Nucleation to Microstructural Features

Crystallographic features at the crack nucleation site, obtained from fatigue experiments on Ti-6242 in [17] are reported in Table 2. This data can be used to capture the effect of local variations in microstructural features on the number of cycles to fatigue crack nucleation. Grains are distinguished as hard or soft, based on their  $\langle c \rangle$ -axis orientation with respect to the loading axis. Orientations between  $0^\circ$  and  $30^\circ$  ensures that the maximum prismatic and basal  $\langle a \rangle$  Schmid factors are in the range 0.0–0.1 and 0.3–0.45, respectively.

The  $\langle c \rangle$ -axis orientation at the crack nucleation site for specimen 1 is predicted to be  $38.5^\circ$  by the crack nucleation model. Consequently, a  $\langle c \rangle$ -axis orientation range of  $0\text{--}40^\circ$  is used here to identify hard and soft grains. A grain is assumed to be hard when its  $\langle c \rangle$ -axis orientation with respect to the loading direction is less than  $40^\circ$ . Since hard grains surrounded by soft grains are more susceptible to crack nucleation, the surface area fraction of soft grains surrounding each hard grain or SAFSSG is examined as a potential metric. The distribution of SAFSSG for specimens 1–3 is shown in Fig. 10.

The number of cycles to crack nucleation depends on the extreme values of the distribution in Fig. 10. This implies that a microstructure with a higher volume fraction of hard grains with high SAFSSG is likely to nucleate cracks earlier. Figure 10 illustrates that specimen 2 should have the longest nucleation life and specimen 3 should have the shortest life. This observation is supported by dwell

**Fig. 10** Volume fraction distribution of hard grains and corresponding surface area fractions of surrounding soft grains (SAFSSG) in specimens 1–3



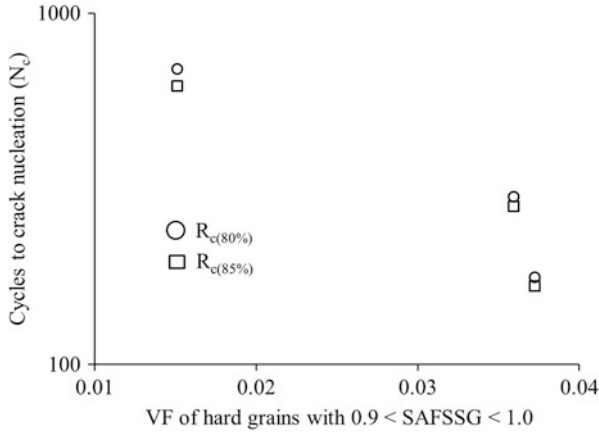


**Fig. 11** Comparison of number of cycles to crack nucleation for different volume fraction (VF) of hard grains with surface area fraction of surrounding soft grains (SAFSSG) between 0.9 and 1

fatigue simulations and experiments for specimens 1 and 2. A comparison of cycles to crack nucleation for different volume fraction (VF) of hard grains with increasing surface area fraction *SAFSSG* between 0.9 and 1 is shown in Fig. 11.

## 5.2 Sensitivity of Crack Nucleation to Characteristics of Applied Loading

Specimen 3 is subjected to four different loading cases for this sensitivity study, viz.:

- Case A:  $\sigma_{max} = 894$  MPa,  $\sigma_r = 0$ ,  $T_{load} = T_{unload} = 1$  s and  $T_{hold} = 120$  s
- Case B:  $\sigma_{max} = 847$  MPa,  $\sigma_r = 0$ ,  $T_{load} = T_{unload} = 1$  s and  $T_{hold} = 120$  s
- Case C:  $\sigma_{max} = 894$  MPa,  $\sigma_r = 0$ ,  $T_{load} = T_{unload} = 61$  s and  $T_{hold} = 0$  s
- Case D:  $\sigma_{max} = 894$  MPa,  $\sigma_r = 0$ ,  $T_{load} = T_{unload} = 1$  s and  $T_{hold} = 0$  s

The maximum applied stress  $\sigma_{max}$  is 95% of yield strength for cases A, C, and D, while it is 90% for case B. Dwell load with 2 min hold is applied in cases A and B. Triangular loading with time periods  $T = 122$  s and  $T = 2$  s are respectively applied for cases C and D. The WATMUS method is used to perform cyclic CPFEM simulations and the crack nucleation parameter  $R_\alpha$  is evaluated at nodes on the grain boundaries. Within a cycle,  $R_\alpha$  is evaluated at the beginning of unloading. This corresponds to  $\tau = 121$  s for cases A and B,  $\tau = 61$  s for case C and  $\tau = 1$  s for case D. The evolution of  $R_\alpha$  at the node, where crack nucleation is predicted, is shown in Fig. 12. The predicted number of cycles to crack nucleation based on the calibrated  $R_c$  values are summarized in Table 3. The microstructure has a shorter life when subjected to dwell loading cases A and B in comparison with normal cyclic



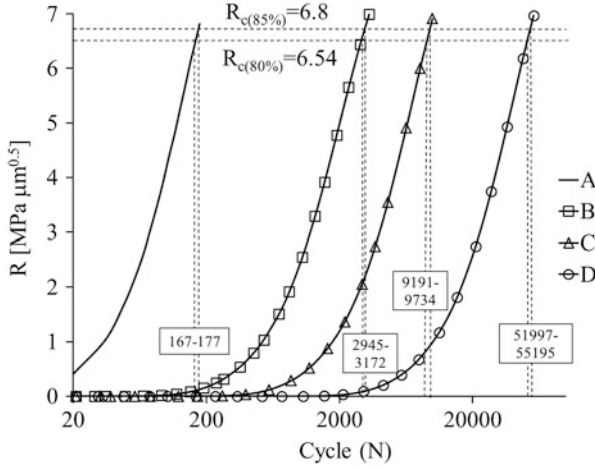


**Fig. 12** Evolution of  $R_c$  with cycles at the predicted crack nucleation site for specimen 3, under four different fatigue loading cases described in Sect. 5.2

**Table 3** Comparison of number of cycles to crack nucleation in specimen 3 for different cyclic loadings

Case no.	Cycles to crack nucleation	
	80 % of life	85 % of life
A	167	177
B	2945	3172
C	9191	9734
D	51,997	55,195

loading cases C and D. For the latter cases, a decrease in loading frequency reduces life. The number of cycles to crack nucleation for dwell case A and normal fatigue case D at 95 % of yield strength shows the same trend as observed experimentally in [2, 17].

In every dwell cycle, the microstructure is held at the maximum stress level for a longer period of time than in the normal cyclic loading. This results in a larger inelastic deformation and strain accumulation in the microstructure within each dwell cycle. Stress concentration and micro-crack growth at the hard soft grain interface are more pronounced in every cycle for the dwell loading. This explains the reduction in life to crack nucleation under dwell load of case A when compared to normal cyclic load of case D. A reduction in the maximum applied stress in dwell loading for case B reduces the cyclic strain accumulation and the accompanying stress rise. Consequently, it shows a longer life than case A. When the frequency of normal cyclic loading is reduced in case C, ramping to the maximum applied stress in every cycle happens slowly. This results in increased plastic strain accumulation and stress rise, compared to the higher frequency case D. Thus, frequency reduction for the same maximum stress level decreases the nucleation life of the microstructure.

The number of cycles to crack nucleation for specimen 3 for different hold, loading, and unloading times in dwell cyclic loading are also compared. The applied stress levels are kept at  $\sigma_{max} = 894$  MPa and  $\sigma_{min} = 0$  MPa, while the total period of loading is  $T = 122$  s. The WATMUS based CPFEM simulations are performed for three different cases, viz.:

- Case E:  $T_{load} = T_{unload} = 16$  s and  $T_{hold} = 90$  s
- Case F:  $T_{load} = T_{unload} = 31$  s and  $T_{hold} = 60$  s
- Case G:  $T_{load} = T_{unload} = 46$  s and  $T_{hold} = 30$  s

The number of cycles to nucleate a crack is evaluated and the nodal  $R_\alpha$  at the predicted crack nucleation site is evaluated at  $\tau = 106$  s, 91 s, and 76 s, respectively within the cyclic increments. The number of cycles to crack nucleation for cases E, F and G are summarized in Table 4. A comparison of the number of cycles to crack nucleation for different hold times is shown in Fig. 13.

**Table 4** Number of cycles to crack nucleation in specimen 3 for dwell cyclic load with different hold times

Case no.	Cycles to crack nucleation	
	80 % of life	85% of life
E	247	261
F	364	394
G	690	755

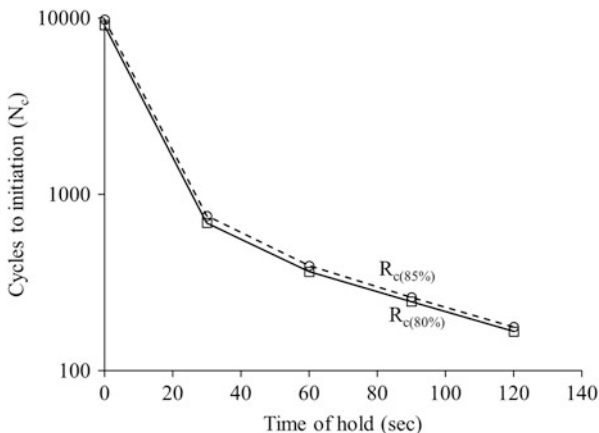


**Fig. 13** Number of cycles to crack nucleation in specimen 3 for different hold times

## 6 Conclusion

This chapter investigates the effects of critical morphological and crystallographic characteristics of the microstructure and loading conditions on grain-level crack nucleation in polycrystalline Ti-6242 microstructures. Crystal plasticity FEM simulations of statistically equivalent microstructures, in conjunction with a physically motivated crack nucleation model, are used to provide a mechanistic approach towards predicting this behavior. A non-local crack nucleation model in terms of the local stresses near the hard grain boundary and the piled-up dislocations in the adjacent soft grain is implemented to predict nucleation in the hard grain. Crack nucleates when a parameter  $R$  at any node on hard soft grain interfaces exceeds a critical value  $R_c$  for the material. A necessary ingredient of cyclic simulations is the wavelet transformation induced multi-time scaling or WATMUS algorithm for accelerated cyclic CPFEM simulations.

Crack nucleation studies are performed for cyclic loads with the maximum applied stress levels at 90–95 % of the macroscopic yield strength. To understand the effect of microstructural characteristics on the fatigue crack nucleation behavior, the dependence of yield strength on the underlying grain orientations and sizes is developed through the introduction of an effective microstructural parameter *Plastic Flow Index* or *PFI*. The *PFI* distribution is found to provide a good measure of the yield strength for a microstructure. However, this distribution is not suitable to undermine the effects of the microstructure on crack nucleation, since it is a *local* event. Hence a local microstructural variable is defined in terms of the neighborhood of the hard grains. Specifically the surface area fraction of soft grains surrounding each hard grain or *SAFSSG* is used to establish the microstructural sensitivity of cycles to crack nucleation. The WATMUS-based CPFEM simulations of three representative microstructures are performed under cyclic dwell loading and the cycles to crack nucleation are predicted. The results confirm the effectiveness of the *SAFSSG* in capturing the influence of microstructure on cycles to crack nucleation. Furthermore, simulations with different cyclic load patterns suggest that fatigue crack nucleation in Ti-6242 strongly depends on the dwell cycle hold time at maximum stress. This is in compliance with experimental observations.

**Acknowledgements** This work has been partially supported by the Air Force Office of Scientific through a grant FA9550-13-1-0062 (Program Manager: Dr. David Stargel) and by the National Science Foundation, Mechanics and Structure of Materials Program through Grant No. CMMI-1100818 (Program Manager: Dr. Thomas Siegmund). This sponsorship is gratefully acknowledged.

## References

1. Anahid M, Samal MK, Ghosh S (2011) Dwell fatigue crack nucleation model based on crystal plasticity finite element simulations of polycrystalline Titanium alloys. *J Mech Phys Solids* 59(10):2157–2176
2. Bache MR (2003) A review of dwell sensitive fatigue in titanium alloys: the role of microstructure, texture and operating conditions. *Int J Fatigue* 25:1079–1087
3. Bridiera F, McDowell DL, Villechaisea P, Mendez J (2009) Crystal plasticity modeling of slip activity in Ti-6Al-4V under high cycle fatigue loading. *Int J Plast* 25:1066–1082
4. Chakraborty P, Ghosh S (2013) Accelerating cyclic plasticity simulations using an adaptive wavelet transformation based multi-time scaling method. *Int J Numer Methods Eng* 93:1425–1454
5. Chakraborty P, Joseph DS, Ghosh S (2011) Wavelet transformation based multi-time scale crystal plasticity FEM for cyclic deformation in titanium alloys under dwell load. *Finite Elem Anal Des* 47:610–618
6. Deka D, Joseph DS, Ghosh S, Mills MJ (2006) Crystal plasticity modeling of deformation and creep in polycrystalline Ti-6242. *Metall Trans A* 37(5):1371–1388
7. Ghosh S, Chakraborty P (2013) Microstructure and load sensitive fatigue crack nucleation in Ti-6242 using accelerated crystal plasticity FEM simulations. *Int J Fatigue* 48:231–246
8. Goh CH, Wallace JM, Neu RW, McDowell DL (2001) Polycrystal plasticity simulations of fretting fatigue. *Int J Fatigue* 23:5423–5435
9. Groeber M, Ghosh S, Uchic MD, Dimiduk DM (2008) A framework for automated analysis and simulation of 3D polycrystalline microstructures. Part 1: statistical characterization. *Acta Mater* 56:1257–1273
10. Groeber M, Ghosh S, Uchic MD, Dimiduk DM (2008) A framework for automated analysis and simulation of 3D polycrystalline microstructures. Part 2: synthetic structure generation. *Acta Mater* 56:1274–1287
11. Hasija V, Ghosh S, Mills MJ, Joseph DS (2003) Modeling deformation and creep in Ti-6Al alloys with experimental validation. *Acta Mater* 51:4533–4549
12. Joseph DS, Chakraborty P, Ghosh S (2010) Wavelet transformation based multi-time scaling for crystal plasticity FE simulations under cyclic loading. *Comput Methods Appl Mech Eng* 199:2177–2194
13. McDowell D, Dunne FPE (2010) Microstructure-sensitive computational modeling of fatigue crack formation. *Int J Fatigue* 32:1521–1542
14. Mineur M, Villechaise P, Mendez J (2000) Influence of the crystalline texture on the fatigue behavior of a 316L austenitic stainless steel. *Mater Sci Eng A* 286:257–268
15. Sackett EE, Germain L, Bache MR (2007) Crystal plasticity, fatigue crack initiation and fatigue performance of advanced titanium alloys. *Int J Fatigue* 29:2015–2021
16. Sinha S, Ghosh S (2006) Modeling cyclic ratcheting based fatigue life of HSLA steels using crystal plasticity FEM simulations and experiments. *Int J Fatigue* 28:1690–1704
17. Sinha V, Mills MJ, Williams JC (2004) Understanding the contributions of normal-fatigue and static loading to the dwell fatigue in a near-alpha titanium alloy. *Metall Mater Trans A* 35:3141–3148
18. Stroh AN (1954) The formation of cracks as a result of plastic flow. *Proc R Soc Lond Ser A* 223:404–414
19. Venkatramani G, Ghosh S, Mills MJ (2007) A size-dependent crystal plasticity finite element model for creep and load-shedding in polycrystalline Titanium alloys. *Acta Mater* 55:3971–3986
20. Williams JC (2006) The evaluation of cold dwell fatigue in Ti-6242. FAA report. The Ohio State University